J. Chil. Chem. Soc., 69, N°1 (2024)

SYNTHESIS AND APPLICATION OF MIXED SPINEL $Mn_{0.4}Cd_{0.6}Cr_2S_2Se_2$: STRUCTURAL, MAGNETIC, AND ELECTROCHEMICAL SENSING PROPERTIES

C. BARRIENTOS [1], P. BARAHONA [2], A. GALDÁMEZ [3], C. CORTÉS [3] AND S. MORIS [1]*

[1] Centro de Investigación de Estudios Avanzados del Maule (CIEAM), Vicerrectoría de Investigación y Postgrado, Universidad Católica del Maule, Avenida San Miguel 3605, Talca 3480112, Chile.
[2]Facultad de Ciencias Básicas, Universidad Católica del Maule, Avenida San Miguel 3605, Talca 3480112, Chile.
[3]Facultad de Ciencias, Departamento de Química, Universidad de Chile, Avenida Las Palmeras 3425, Santiago 7800003, Chile.

ABSTRACT

Herein we report the solid synthesis, structural characterization, magnetic behavior, and electrochemical sensing properties of $Mn_{0.4}Cd_{0.6}Cr_2S_2Se_2$. Single-crystal X-ray diffraction analysis showed that $Mn_{0.4}Cd_{0.6}Cr_2S_2Se_2$ crystallizes in a spinel-type structure. Powder X-ray diffraction patterns and Rietveld refinement data revealed that this selenide phase is consisted of cubic $Fd\overline{3}m$ space group. Magnetic field cooling (MFC) measurements indicated an enhancement in ferromagnetic interactions relative to the ferrimagnetic compound $Mn_{0.4}Cd_{0.6}Cr_2S_4$, which can be attributed to the substitution of sulphur by selenium. The electrochemical response of modified glassy carbon electrodes with $Mn_{0.4}Cd_{0.6}Cr_2S_2Se_2$ was increased, the peak current is increased 4-fold, from 20.15 µA to 83.52 for GC, and GC-$Mn_{0.4}Cd_{0.6}Cr_2S_2Se_2$ respectively by differential pulse voltammetry, and thus it could be used to design an electrochemical sensor to quantify nitrocompounds, considered pollutants and toxic agents for humans, plants, and animals.

Keywords: Chalcospinel, electrochemical sensor, ferromagnetism, single crystal.

1. INTRODUCTION

The use of magnetic materials in electrochemical detection has a great potential for detecting and performing various analyses. This is due to the special properties of magnetic materials, which can enhance the efficacy and sensitivity of electrochemical sensors[1]. These materials can be used to identify biological components, pollutants in the environment, and chemical species, among other analyses[2,3]. Mainly oxides have been used as sensors for various species, such as, whether environmental pollutants[4], drugs[5], volatile organic compounds (VOCs)[6] and nitro aromatic compounds (NACs)[7–9], among others[10–14] , but it has been demonstrated in some cases that sulfides have richer redox reactions as well as higher conductivity, they have the ability to offer multiple reaction sites, extended mass and charge transport channels, and elevated surface-to-volume ratios[12,15–17]. Furthermore, they outperform metal oxides in terms of mechanical, thermal, and electrical conductivities[17–19].

These oxides materials correspond to spinels that are a large group of compounds having the general structure $(A)[B_2]X_4$, with the same crystal structure as the natural mineral $MgAl_2O_4$, $Fd\overline{3}m$ (227), where the square brackets indicate the octahedral sites and the parenthesis indicate the tetrahedral ones (e.g., examples ACr_2X_4, A = Mn, Fe, Co, Cu, Zn, and often X are O^{2-}, S^{2-}, Se^{2-}, or Te^{2-} [20–28]). Over time, more than 200 distinct spinels with the general formula AB_2X_4 have been discovered or produced in single- or polycrystalline form and they became significant early on as ferromagnetic or ferrimagnetic insulators with high ordering temperatures and rather high saturation magnetization[21]. Has been found, electrical conductivities of chalcospinels (AB_2X_4 with X = S^{2-}or Se^{2-}), mechanical and thermal stabilities are superior to those of their corresponding metal oxides[17] and modeling the magnetic properties of these spinels is achieved by replacing the cations and chalcogen that make them up. There are various synthesis methods to obtain chalcospinels, but the conventional ceramic method can be advantageous owing to its simple operation, low cost, high yield, and bulk production[29,30]. Allowing its direct use in different applications such as the substances electrochemical quantification.

On the other hand, Nitrophenol (NP) derivatives are compounds extensively used in industry, and they are considered toxic agents for humans, plants, and animals[31–33]. 4-Nitrophenol (4-NP) is the most common and abundant of nitrophenol compounds, thus, it is important to develop strategies to quantify this analyte[34]. There are several methodologies for 4-NP quantification, Liquid Chromatography, UV-vis Spectrophotometry, and Chemiluminescence, with good performances, but with a high cost, limiting their use[35]. As an alternative, the electrochemical methods to quantify 4-NP have the advantage of lower cost, easier operation, and short-time response, compared with the above-mentioned, and this is the reason the developing of sensors with new materials that improve electrochemical response is an interesting field to investigate[36,37].

In this work, we present the synthesis, structural, and magnetic characterization of $Mn_{0.4}Cd_{0.6}Cr_2S_2Se_2$, as well as the study on the reduction of 4-Nitrophenol (4-NP) for promising candidate for the design of electrochemical sensors for the quantification of nitrocompounds using magnetic mixed chalcospinels.

2.EXPERIMENTAL SECTION

2.1 Materials

All the reagents used for the synthesis of these compounds were obtained commercially from Sigma-Aldrich, St. Louis, USA, and used without further purification.

2.2 Synthesis

Polycrystalline $Mn_{0.4}Cd_{0.6}Cr_2S_2Se_2$ compounds were prepared using ceramic method at high temperature by directly combining high-purity elemental powders (99.99%, Aldrich) in stoichiometric amounts. All manipulations were carried out under an argon atmosphere. The reaction mixtures were sealed in evacuated quartz ampoules and placed in a programmable furnace. The ampoules were then slowly heated from room temperature to 800 °C at 60 °C/h and held at the maximum temperature for 8 days, then ampoules were cooled to room temperature to be opened and ground the sample, resealed, and heated again to 800 °C at 60 °C/h for 8 days more. Finally, the ampoules were cooled to room temperature, they were opened and ground for further characterization.

2.3 Characterization

2.3.1 Powder X-ray diffraction measurements

Powder X-ray diffraction (PXRD) patterns were collected at room temperature on Bruker D8 Advance diffractometer equipped with a Cu Kα radiation source, in a range the range $5° < 2\theta < 80$. The XRD patterns were indexed using the CHEKCELL software [38]. The collected data were analyzed by Fullprof Rietveld refinement software [39]. A LaB_6 powder standard was used to determine the instrumental profile.

2.3.2 Single Crystal X-ray Diffraction

Single-crystal X-ray diffraction (XRD) data for $Mn_{0.4}Cd_{0.6}Cr_2S_2Se_2$ were recorded at RT with a D8 Venture Bruker AXS diffractometer equipped with MoKα radiation (λ= 0.71073 Å). Data were accumulated using the Bruker SMART software package[40]. Structural refinement was performed using the SHELXL [41] and Olex2[42] programs.

*Corresponding author email: smoris@ucm.cl

2.3.3 Magnetic Measurements

Magnetic measurements were performed on pelletized powder samples using a physical property measurement system (PPMS-9T), manufactured by Quantum Design, in a temperature range from 5 K to 300 K. Continuous susceptibility $\chi dc(T) = M(T)/H$ measurements were obtained for magnetization field cooling (MFC) with applied magnetic field H = 0.05 T.

2.3.4 Electrochemical Measurements

Electrochemical measurements were performed with a potentiostat CHI650E from CH Instruments, USA.

A three-electrode arrangement cell with PBSx10 at pH 7.44 was used. Glassy carbon electrode, GC, (GC CH Instruments CHI104) as a working electrode, Ag/AgCl (CHI111 3 M KCl) as a reference electrode, and Pt wire (CHI115) as a counter electrode. The cell was purged with Nitrogen for 15 minutes before the electrochemical measurements, and the pressure was maintained during all experiments.

Electrode modification

Glassy carbon electrodes were previously polished with 0.3 and 0.05 µm alumina and then washed with deionized water and dried at room temperature to be modified using a drop cast technique with an aliquot of 20 µL of 3 mg/mL of $Mn_{0.4}Cd_{0.6}Cr_2S_2Se_2$ dispersion in isopropanol onto the electrode surface. The modified electrodes were allowed to air dry at room temperature to obtain GC-$Mn_{0.4}Cd_{0.6}Cr_2S_2Se_2$ electrodes.

4-Nitrophenol quantification

Using the electrochemical cell conditions mentioned before, the addition of 4-nitrophenol, 4-NP, was performed to evaluate the GC-$Mn_{0.4}Cd_{0.6}Cr_2S_2Se_2$ electrode used as a possible sensor for nitro compounds.

3. RESULTS AND DISCUSSION

3.1. X-ray powder diffraction and compositional characterization

The crystal structure of $Mn_{0.4}Cd_{0.6}Cr_2S_2Se_2$ was resolved by single-crystal X-ray diffraction in the cubic $Fd\overline{3}m$ space group. The least-squares refinement of the occupation factors and the displacement parameters converged to a model in which the tetrahedral (A) positions were occupied by Cd and Mn (8a Wyckoff sites) and the octahedral [B] positions (16d Wyckoff sites) were occupied by Cr. The S and Se atoms occupy the 32e (*u*,*u*,*u*) Wyckoff sites in a cubic closed-packed array. This model was based on linear functions constraining the Mn, Cd, and Cr atoms at the 8a and 16d sites. The sum of the site occupation factor (SOF) was forced to equal 1 (fully occupied for $8a = (1 - x)Mn + xCd$. Furthermore, for the chalcogenide site, the sum of the SOF was forced to equal 1 (fully occupied) for $32e = (4 - y)S + ySe$, and the Mn/Cd and S/Se atoms were also constrained to have equivalent atomic displacement parameters (ADPs). The detailed crystallographic data and refinement results are summarized in Tables 1.

Table 1. Crystallographic data and structure refinement details CSD-2368795.

Empirical formula	$Mn_{0.40}Cd_{0.60}Cr_2S_2Se_2$
Formula weight	413.06
Temperature/K	300
Crystal system	cubic
Space group	$Fd\overline{3}m$
a/Å	10.4157(5)
b/Å	10.4157(5)
c/Å	10.4157(5)
α/°	90
β/°	90
γ/°	90
Volume/Å^3	1129.97(16)
Z	8
$\rho_{calc}g/cm^3$	4.916
μ/mm^{-1}	20.434
F(000)	1503
Crystal size/mm^3	0.05 × 0.045 × 0.022
Radiation	MoKα (λ = 0.71073)
2Θ range for data collection/°	6.776 to 60.65
Index ranges	$-14 \leq h \leq 14, -14 \leq k \leq 14, -14 \leq l \leq 14$
Reflections collected	5229
Independent reflections	108 [$R_{int} = 0.0954$, $R_{sigma} = 0.0228$]
Data/restraints/parameters	108/0/8
Goodness-of-fit on F^2	1.122
Final R indexes [I>=2σ (I)]	$R_1 = 0.0259$, $wR_2 = 0.0671$
Final R indexes [all data]	$R_1 = 0.0319$, $wR_2 = 0.0721$
Largest diff. peak/hole / e Å^{-3}	0.879/-0.657

The Cr-X (X = Se/S) bond distance in $Mn_{0.40}Cd_{0.60}Cr_2S_2Se_2$ was 2.4824(5) Å which is comparable with other Cr-spinels[29]. Cd/Mn–X (X = Se/S) distance in the sample was 2.4771(10)Å higher than informed for Mn-S distance 2.387 Å in $MnCr_2S_4$ [43] . This is due to the presence of Cd in the Mn site and S in the Se site, both of which have a larger ionic radius, resulting in an increase in the unit cell size. The bond angles of X-Cd/Mn-X is 109.5, bond angle of X-Cr-X (X = Se/S) (180.0, 96.07 and 83.93) in the sample are very similar to the bond angles in $CuCr_{1.1}Sn_{0.9}S_{2.3}Se_{1.7}$ [29](180.0, 92.28 and 87.72). The degrees of distortion of the tetrahedra or octahedra were evaluated using the distortion indices (DI) defined by Baur and Wildnerwil[44–46]. The $Mn_{0.40}Cd_{0.60}Cr_2S_2Se_2$ compound have three-atom centered polyhedral structure: $(A)X_4$ (tetrahedron), $[B]X_6$ (octahedron) and $X[B_3A]$ with A = Mn/Cd, B = Cr and X = S/Se. The degree of distortion in the polyhedral can be measured using the edge length distortion (ELD) indices. The $X[B_3A]$ tetrahedron is the most distorted polyhedron (~8% distortion from an ideal tetrahedron)[47]. These values compare very well with those found for other

Cr-spinels[29]. The (A)X_4 tetrahedra were ideal, with tetrahedral angles 109.5°. The [B]X_6 was slightly distorted indicating a near-ideal octahedral structure.

The XRD pattern was fully indexed in the space group $Fd\overline{3}m$ (N° 227), with the exception of two very weak impurity peaks, within the detection limits of the technique (Figure 1). These peaks correspond to the $MnCr_2S_4$ phase present less than 1% as reported by the Rietveld analysis (Figure 2). Lattice parameters of powder sample calculated by Rietveld refinement are shown in Table 2. The experimental XRD patterns were compared with the simulated XRD patterns derived from the single-crystal XRD data. The shape and intensity of the XRD peaks indicates the high crystallinity, and the observed interlayer spacing was in good agreement with the calculated interplanar spacing *d*.

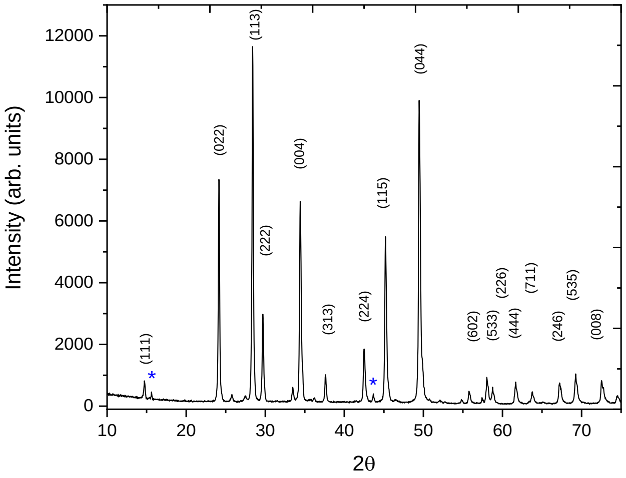

Figure 1. X-ray powder diffraction patterns for $Mn_{0.4}Cd_{0.6}Cr_2S_2Se_2$. The blue asterisks indicate reflections associated with a $MnCr_2S_4$ impurity.

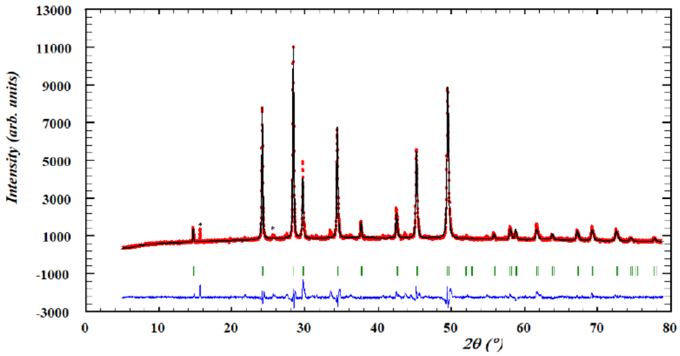

Figure 2. Rietveld refinement of powder diffraction pattern of $Mn_{0.4}Cd_{0.6}Cr_2S_2Se_2$. Black solid line is calculated pattern, red dashed line is experimental data, the green ticks are Bragg positions, and the bottom blue line is the difference of experimental and calculated patterns.

Table 2. Results of Rietveld refinement and agreement factors from powder diffraction data for $Mn_{0.4}Cd_{0.6}Cr_2S_2Se_2$.

Empirical formula	*$Mn_{0.4}Cd_{0.6}Cr_2S_2Se_2$*
Crystal system	Cubic
Space group	$Fd\overline{3}m$
a/Å	10.41648(7)
V/Å³	1130.22(9)
d/g cm⁻³	4.883
Agreement factors	
R_p	5.1
R_{wp}	7.1
χ^2	5.5

Lattice parameter a calculated (10.416 Å) is greater than the system $Mn_{0.4}Cd_{0.6}Cr_2S_4$ (10.192 Å) obtained in 2010 by Barahona and coworkers[30]. This fact could be related to the difference of ion size radii of Se^{2-} (1.98 Å) and S^{2-} ions (1.84 Å), which causes an increase in the network parameters[48]. In addition, this value is close to that reported for the spinel of the $MnCr_2S_2Se_2$ type, which is 10.315 Å[49]. Is important to note that the larger size of Cd^{2+} (0.92 Å) compared to Mn^{2+} (0.80 Å) also affect the cell parameter. Therefore, there is a simultaneous effect of both the chalcogen (Se^{2-}) and the ion-metal (Cd^{2+}). The size of unit cell will increase consequently as substitution of Selenium in the crystallographic sites of Sulphur. The average grain size, which is determined from grazing incidence XRD using the Debye–Scherrer formula[50] with the full width at half maximum of the (022) diffraction peak, is ~45.5 nm.

3.2 Magnetic Measurements

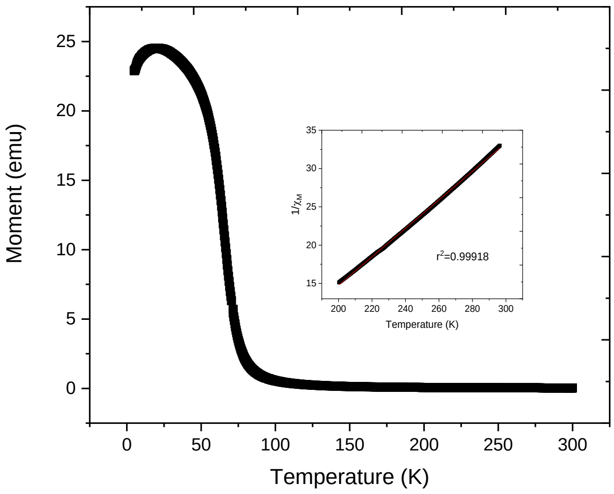

Figure 3. MFC magnetization for $Mn_{0.4}Cd_{0.6}Cr_2S_2Se_2$

The Figure 3 shows MFC measurements on $Mn_{0.4}Cd_{0.6}Cr_2S_2Se_2$, the paramagnetic regime was identified well above the magnetic transition temperature at 500 Oe (inset Figure 3). The inverse susceptibility was fitted by a classical Curie-Weiss relation $c = C/(T-q)$ in the range $200 \leq T \leq 300$K. The effective moment m_{eff} obtained was 6.56 MB, this value agrees with what can be expected for Mn^{2+} and Cr^{3+} free-spin values. The Curie-Weiss temperature was +120 K, this value that indicates a strong ferromagnetic component in the ferrimagnetic behavior of the material.

In our work, we define the paramagnetic to ferrimagnetic transition Tc at the temperature where a change in the slope in MFC of the magnetic measurements occurs, i.e. Tc = 66.1 (±1) K, while T_{max} ~20.6 (±1)K. T_{max} corresponds to a reorientation of the manganese spins in the presence of the internal field created by the ferromagnetic chromium sublattice[30] .

The transition temperature Tc = 66.1 K of $Mn_{0.4}Cd_{0.6}Cr_2S_2Se_2$ should be compared with that obtained in polycrystalline $Mn_{0.4}Cd_{0.6}Cr_2S_4$ (Tc = 79 K). The decrease in the transition temperature from paramagnetic to ferrimagnetic can be associated with the replacement of sulphur with selenium in the structure, similarly to $MnCr_2S_{4-x}Se_x$ where an increase in the amount of selenium causes a decrease in the Tc value from 72 to 63 K for x = 0.1 to 1[49]. With respect to the ferromagnetic interaction parameter, the value +120 K higher compared to +30 K for $MnCr_2S_4$ and +91 ± 5K for $Mn_{0.4}Cd_{0.6}Cr_2S_4$, this can be explained with the increase in the ferromagnetic interactions of the chromium ions due to the replacement of sulphur by selenium, which has a larger size[30].

The magnetic parameters obtained for $Mn_{0.4}Cd_{0.6}Cr_2S_2Se_2$ indicate a stronger ferromagnetism when sulphur is replaced by selenium, this would be due to the fact that the antiferromagnetic interactions between the manganese and chromium sublattices are weakened by the increase in the separation of the magnetic ions, product of the presence of selenium, which is larger than sulphur, leading to well-aligned spins pointing in the same direction[48]. The latter would favour the ferromagnetic interactions of the chromium moments and, on the other hand, the internal field due to the Cr lattice imposes a predominant orientation in the direction of the applied field.

3.3 Cyclic voltammetry

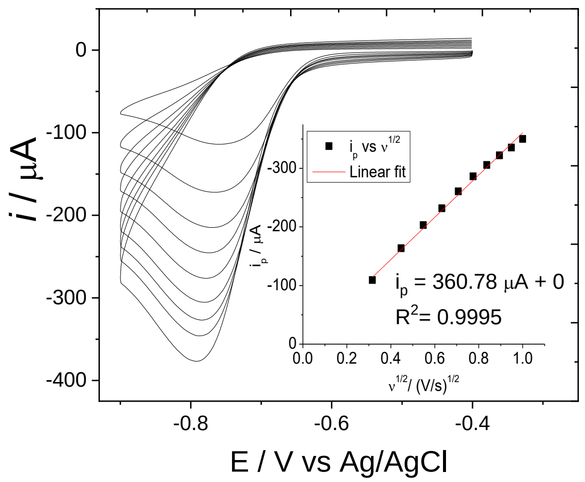

Figure 5. Cyclic voltammetry of 4NP 1 mM in PBS 10X at pH 7.44 at different sweep rates.

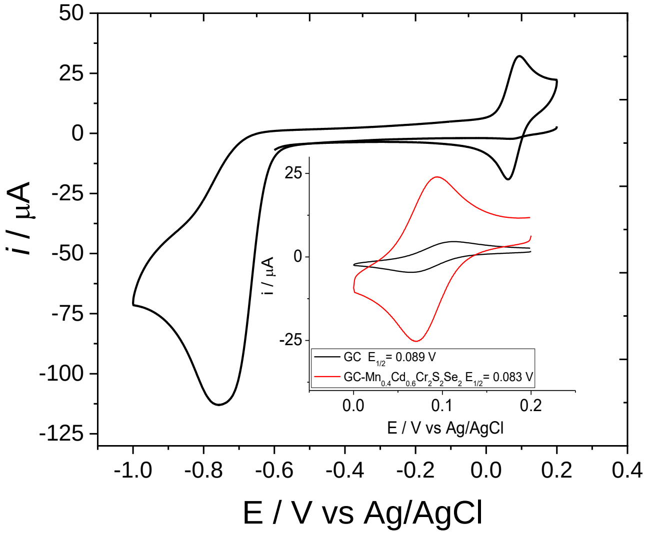

Figure 6. Extended cyclic voltammetry of 4NP 1 mM in PBS 10X at pH 7.44 at 0.1 Vs^{-1}.

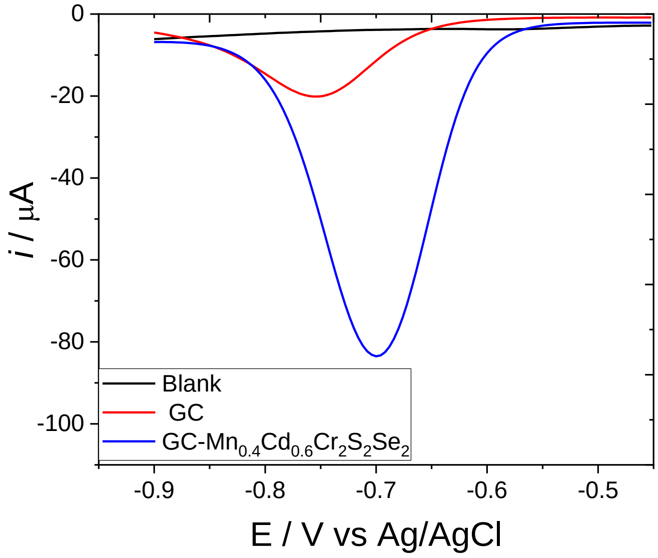

Figure 7. Differential pulse voltammetry of 4NP 1 mM in PBS 10X at pH 7.44

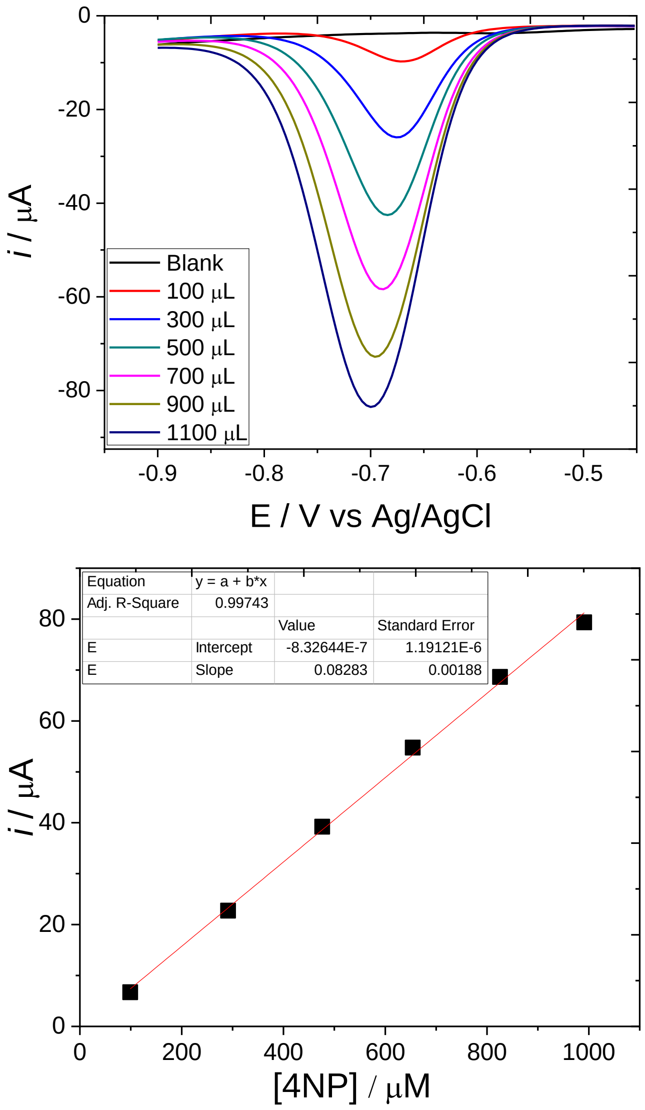

Equation	y = a + b*x		
Adj. R-Square	0.99743		
		Value	Standard Error
E	Intercept	-8.32644E-7	1.19121E-6
E	Slope	0.08283	0.00188

Figure 8. (up) Differential pulse voltammetry at different aliquots of 4NP 0.01 M in PBS 10X at pH 7.44 using GC-$Mn_{0.4}Cd_{0.6}Cr_2S_2Se_2$ and (down) its Calibration curve of DPV.

Figure 5 shows cyclic voltammograms from 0.1 - 1 Vs^{-1} of 4NP 1 mM in PBS for the irreversible reduction process of the –NO_2 group, around at –0.79 V to –NHOH formation is attributed, i_p vs $\upsilon^{1/2}$ was plotted, and the linear tendency indicates the process is diffusion controlled. Subsequently, an extended cyclic voltammogram was performed, Figure 6, and a reversible peak was observed at 0.1 V, corresponding to –NHOH/–NO redox pair, which was isolated in the insert of Figure 6, with a negligible shift in $E_{1/2}$ values (0.089 V, and 0.083 V for GC and GC-$Mn_{0.4}Cd_{0.6}Cr_2S_2Se_2$ respectively). A DPV for comparison between GC and GC-$Mn_{0.4}Cd_{0.6}Cr_2S_2Se_2$ electrodes was made, Figure 8, with a slight shift from -0.753 and -0.700 V peak potential, E_p, respectively was observed. Also, the peak current is increased 4-fold, from 20.15 µA to 83.52 for GC, and GC-$Mn_{0.4}Cd_{0.6}Cr_2S_2Se_2$ correspondingly. These results indicate that $Mn_{0.4}Cd_{0.6}Cr_2S_2Se_2$ is a suitable material to modify electrodes for quantification purposes, thus, the response for -NO_2 reduction by DPV technique was followed, to an increasing concentration of 4-NP, shows an increase in the peak current, Figure 8 left. A calibration curve to assess a possible use as a sensor for this sample was made, and, subsequently, a peak current vs 4-NP concentration was plotted, Figure 8 right, and a good linear tendency was observed in the range of concentration used (99 µM to 0.99 mM) with $R^2 = 0.997$. All these results show that $Mn_{0.4}Cd_{0.6}Cr_2S_2Se_2$ is suitable for develops a sensor for 4-NP detection, this opens possibilities for the use of this material to study many other nitrocompounds, and also test other spinels for this purpose.

CONCLUSIONS

In summary polycrystalline $Mn_{0.4}Cd_{0.6}Cr_2S_2Se_2$ were successfully obtained using ceramic method at high temperature, single crystal was obtained as by-product of synthesis and this structure were confirmed by single crystal x-ray diffraction. MFC measurements on $Mn_{0.4}Cd_{0.6}Cr_2S_2Se_2$ indicates an increase of the ferromagnetic interaction with respect to the ferrimagnetic compound $Mn_{0.4}Cd_{0.6}Cr_2S_4$, when sulphur is replaced by selenium, which presents a larger size. The replacement of the anion causes the antiferromagnetic alignment between the Mn and Cr spins to decrease due to the separation of the ion sublattices. In addition, the sublattice separation causes the chromium ions to impose a predominant preferential orientation in the direction of the applied field leading to an overall ferromagnetic alignment. As we can see, using $Mn_{0.4}Cd_{0.6}Cr_2S_2Se_2$ increases the electrochemical response in modified glassy carbon electrodes, and thus it could be used to design an electrochemical sensor to quantify nitro-compounds or explore with other analytes quantification. The use of this material shows a promissory result to be considered in development of sensor of 4-NP or other environmental pollutants.

ACKNOWLEDGEMENT

Author thanks Dr. Javier Campo from the "*Instituto de Nanociencia y Materiales de Aragón* (INMA)" at the University of Zaragoza for providing the equipment to carry out the magnetic measurements.

REFERENCES

1. Ganesh, K. S.; Gutturu, R. R.; Kang, C. S.; Joo, S. W. Characteristics of Nanoparticles of Mixed Cu–Zn–Mg Spinel Ferrites: A Study of Structural and Electrochemical Attributes. *Ceram Int* **2024**, *50* (4), 6268–6277. https://doi.org/10.1016/j.ceramint.2023.11.352.
2. Qin, H.; He, Y.; Xu, P.; Huang, D.; Wang, Z.; Wang, H.; Wang, Z.; Zhao, Y.; Tian, Q.; Wang, C. Spinel Ferrites (MFe_2O_4): Synthesis, Improvement and Catalytic Application in Environment and Energy Field. *Advances in Colloid and Interface Science*. Elsevier B.V. August 1, 2021, pp 1–22. https://doi.org/10.1016/j.cis.2021.102486.
3. Nguyen, V. C.; Kim, H. Spinel Nanoparticles $ZnCo_2O_4$ as High Performance Electrocatalyst for Electrochemical Sensing Antibiotic Chloramphenicol. *Journal of Electrochemical Science and Technology* **2024**, *15* (1), 152–160. https://doi.org/10.33961/jecst.2023.00486.
4. Gonçalves, J. M.; de Faria, L. V.; Nascimento, A. B.; Germscheidt, R. L.; Patra, S.; Hernández-Saravia, L. P.; Bonacin, J. A.; Munoz, R. A. A.; Angnes, L. Sensing Performances of Spinel Ferrites MFe_2O_4 (M = Mg, Ni, Co, Mn, Cu and Zn) Based Electrochemical Sensors: A Review. *Analytica Chimica Acta*. Elsevier B.V. November 15, 2022. https://doi.org/10.1016/j.aca.2022.340362.
5. Palpandi, K.; Bhuvaneswari, C.; Babu, S. G.; Raman, N. Rational Design of Ruddlesden-Popper Phase Mn_2SnO_4 for Ultra-Sensitive and Highly Selective Detection of Chloramphenicol in Real-Life Samples. *New Journal of Chemistry* **2022**. https://doi.org/10.1039/d2nj00813k.
6. Ma, X.; Xiao, M.; Yang, X.; Guo, Y.; Yu, X.; Ge, M. Tuning Benzene Activity of Cobalt-Based Spinel Catalysts with Cation Substitution. *Catal Today* **2024**, *436*. https://doi.org/10.1016/j.cattod.2024.114770.
7. Khan, M. Z. H.; Zhu, J.; Liu, X. Reduced Graphene Oxide-Conjugated Urchin-like $NiCo_2O_4$ Nanostructures for Individual Detection of o-Nitro and p-Amino Phenol. *ACS Omega* **2019**, *4* (7), 11433–11439. https://doi.org/10.1021/acsomega.9b00804.
8. Ramu, A. G.; Salla, S.; Gopi, S.; Silambarasan, P.; Yang, D. J.; Song, M. J.; Ali, H. M.; Salem, M. Z. M.; Choi, D. Surface-Tuned Hierarchical ɤ-Fe_2O_3–N-RGO Nanohydrogel for Efficient Catalytic Removal and Electrochemical Sensing of Toxic Nitro Compounds. *Chemosphere* **2021**, *268*. https://doi.org/10.1016/j.chemosphere.2020.128853.
9. Zhang, J.; Cui, S.; Ding, Y.; Yang, X.; Guo, K.; Zhao, J. T. Two-Dimensional Mesoporous $ZnCo_2O_4$ Nanosheets as a Novel Electrocatalyst for Detection of o-Nitrophenol and p-Nitrophenol. *Biosens Bioelectron* **2018**, *112*, 177–185. https://doi.org/10.1016/j.bios.2018.03.021.
10. Laganovsky, A. V.; Kormosh, Z. O.; Sachanyuk, V. P.; Parasyuk, O. V. Quaternary Thiospinel $CuCrTiS_4$ as an Electroactive Material for Copper(II)-Sensitive and Selective Electrode. *Materials Science and Engineering C* **2008**, *28* (7), 1112–1116. https://doi.org/10.1016/j.msec.2007.05.002.
11. Balamurugan, K.; Rajakumaran, R.; Chen, S. M.; Karthik, R.; Shim, J. J.; Shafi, P. M. Massive Engineering of Spinel Cobalt Tin Oxide/Tin Oxide-Based Electrocatalyst for the Selective Voltammetric Determination of Antibiotic Drug Furaltadone in Water Samples. *J Alloys Compd* **2021**, *882*. https://doi.org/10.1016/j.jallcom.2021.160750.
12. Chen, T. W.; Tamilalagan, E.; Chen, S. M.; Akilarasan, M.; Maheshwaran, S.; Liu, X. An Ultra-Sensitive Electrochemical Sensor for the Detection of Carcinogen Oxidative Stress 4nitroquinoline N-Oxide in Biologic Matrices Based on Hierarchical Spinel Structured $NiCo_2O_4$ and $NiCo_2S_4$; a Comparative Study. *Int J Mol Sci* **2020**, *21* (9). https://doi.org/10.3390/ijms21093273.
13. Palpandi, K.; Raman, N. Electrochemical Detection of 2-Nitroaniline at a Novel Sphere-like Co_2SnO_4 Modified Glassy Carbon Electrode. *New Journal of Chemistry* **2020**, *44* (20), 8454–8462. https://doi.org/10.1039/d0nj01098g.
14. Koventhan, C.; Vinothkumar, V.; Chen, S. M. Development of an Electrochemical Sensor Based on a Cobalt Oxide/Tin Oxide Composite for Determination of Antibiotic Drug Ornidazole. *New Journal of Chemistry* **2021**, *45* (28), 12593–12605. https://doi.org/10.1039/d1nj01345a.
15. Zhao, Q.; Yan, Z.; Chen, C.; Chen, J. Spinels: Controlled Preparation, Oxygen Reduction/Evolution Reaction Application, and Beyond. *Chemical Reviews*. American Chemical Society August 9, 2017, pp 10121–10211. https://doi.org/10.1021/acs.chemrev.7b00051.
16. Shen, J.; Dong, P.; Baines, R.; Xu, X.; Zhang, Z.; Ajayan, P. M.; Ye, M. Controlled Synthesis and Comparison of $NiCo_2S_4$/Graphene/2D TMD Ternary Nanocomposites for High-Performance Supercapacitors. *Chemical Communications* **2016**, *52* (59), 9251–9254. https://doi.org/10.1039/c6cc03699f.
17. Bulakhe, R. N.; Ryu, C.; Gunjakar, J. L.; In, J. Bin. Chemical Route to the Synthesis of Novel Ternary $CuCr_2S_4$ Cathodes for Asymmetric Supercapacitors. *J Energy Storage* **2022**, *56*. https://doi.org/10.1016/j.est.2022.106175.
18. Yu, X. Y.; (David) Lou, X. W. Mixed Metal Sulfides for Electrochemical Energy Storage and Conversion. *Advanced Energy Materials*. Wiley-VCH Verlag January 25, 2018. https://doi.org/10.1002/aenm.201701592.
19. Yu, Z.; Tetard, L.; Zhai, L.; Thomas, J. Supercapacitor Electrode Materials: Nanostructures from 0 to 3 Dimensions. *Energy and Environmental Science*. Royal Society of Chemistry March 1, 2015, pp 702–730. https://doi.org/10.1039/c4ee03229b.
20. Abbasi, J.; Regmi, S.; Gupta, A. Ferromagnetic $Cd_{(1-x)}Cu_xCr_2S_4$ Thin Films: Synthesis, Characterization, and First-Principles Calculations. *J Magn Magn Mater* **2022**, *562*. https://doi.org/10.1016/j.jmmm.2022.169771.
21. Tsurkan, V.; Krug von Nidda, H. A.; Deisenhofer, J.; Lunkenheimer, P.; Loidl, A. On the Complexity of Spinels: Magnetic, Electronic, and Polar Ground States. *Physics Reports*. Elsevier B.V. September 3, 2021, pp 1–86. https://doi.org/10.1016/j.physrep.2021.04.002.
22. Ohgushi, K.; Okimoto, Y.; Ogasawara, T.; Miyasaka, S.; Tokura, Y. Magnetic, Optical, and Magnetooptical Properties of Spinel-Type ACr_2X_4 (A = Mn, Fe, Co, Cu, Zn, Cd; X = O, S, Se). *J Physical Soc Japan* **2008**, *77* (3). https://doi.org/10.1143/JPSJ.77.034713.
23. Valencia-gálvez, P.; Peña, O.; Moris, S.; Barahona, P. RAMAN CHARACTERIZATION OF $CuCr_{2-x}Sn_xS_4$ SPINELS. *J. Chil. Chem. Soc* **2019**, *64* (1), 4285–4289. https://doi.org/10.4067/s0717-97072019000104285.
24. Ozel, F.; Kılıc, H. S.; Coskun, H.; Deveci, I.; Sarılmaz, A.; Balıkcıoglu, A.; Gundogdu, Y.; Aljabour, A.; Ozen, A.; Gezgin, S. Y.; Houimi, A.; Yar, A.; Kus, M.; Ersoz, M. A General Review on the Thiospinels and Their Energy Applications. *Mater Today Energy* **2021**, *21*, 100822. https://doi.org/https://doi.org/10.1016/j.mtener.2021.100822.
25. Barahona, P.; Galdámez, A.; López-Vergara, F.; Manríquez, V.; Peña, O. Crystal Structure and Magnetic Properties of Titanium-Based $CuTi_{2-x}M_xS_4$ and $CuCr_{2-x}Ti_xSe_4$ Chalcospinels. *J Solid State Chem* **2014**, *212*, 114–120. https://doi.org/10.1016/j.jssc.2014.01.017.
26. Moris, S.; Valencia-Gálvez, P.; Mejía-López, J.; Peña, O.; Barahona, P.; Galdámez, A. $(Cu)_{Tet}(Cr_{2-x}Sn_x)_{Oct}S_{4-y}Se_y$ Spinels: Crystal Structure, Density Functional Theory Calculations, and Magnetic Behavior. *Inorg Chem* **2019**, *58* (20), 13945–13952. https://doi.org/10.1021/acs.inorgchem.9b01853.
27. Pinto, C.; Galdámez, A.; Barahona, P.; Moris, S.; Peña, O. Crystal Structure, Raman Scattering and Magnetic Properties of $CuCr_{2-x}Zr_xSe_4$ and $CuCr_{2-x}Sn_xSe_4$ Selenospinels. *J Magn Magn Mater* **2018**, *456*, 160–166. https://doi.org/10.1016/j.jmmm.2018.02.023.
28. Moris, S.; Barahona, P.; Galdámez, A. Crystal Structure of $(Cu_{0.51}In_{0.49})_{Tet}[Cr_{1.74}In_{0.26}]_{Oct}Se_4$ Selenospinel, $Cu_{0.51}In_{0.75}Cr_{1.74}Se_4$. *Zeitschrift für Kristallographie-New Crystal structure* **2019**, *234* (3), 421–422. https://doi.org/10.1515/ncrs-2018-0426.
29. Valencia-gálvez, P.; Aravena, D.; Barahona, P.; Moris, S.; Galdámez, A. Effects of Tin and Sulfur Chemical Substitution on the Structural and

Electrical Properties of $CuCr_2Se_4$ Selenospinel. *Applied Sciences (Switzerland)* **2022**, *12* (3). https://doi.org/10.3390/app12031586.

30. Barahona, P.; Galdamez, A.; Manríquez, V.; Cruzat, C.; Raison, C.; Le Coz, S.; Peña, O.; Moure, C. Effect of Cation Substitution on Magnetic Properties in $Mn_{1-X}A'_xCr_2S_4$ (A' = Cd, Zn) Thiospinel Series. *Advances in Applied Ceramics* **2010**, *109* (7), 431–435. https://doi.org/10.1179/174367609X414125.
31. Abdel-Aziz, A. M.; Hassan, H. H.; Badr, I. H. A. Activated Glassy Carbon Electrode as an Electrochemical Sensing Platform for the Determination of 4-Nitrophenol and Dopamine in Real Samples. *ACS Omega* **2022**, *7* (38), 34127–34135. https://doi.org/10.1021/acsomega.2c03427.
32. Zeng, Y.; Zhou, Y.; Zhou, T.; Shi, G. A Novel Composite of Reduced Graphene Oxide and Molecularly Imprinted Polymer for Electrochemical Sensing 4-Nitrophenol. *Electrochim Acta* **2014**, *130*, 504–511. https://doi.org/10.1016/j.electacta.2014.02.130.
33. Zhang, J.; Cui, S.; Ding, Y.; Yang, X.; Guo, K.; Zhao, J. T. Two-Dimensional Mesoporous $ZnCo_2O_4$ Nanosheets as a Novel Electrocatalyst for Detection of o-Nitrophenol and p-Nitrophenol. *Biosens Bioelectron* **2018**, *112*, 177–185. https://doi.org/10.1016/j.bios.2018.03.021.
34. Thirumalraj, B.; Rajkumar, C.; Chen, S. M.; Lin, K. Y. Determination of 4-Nitrophenol in Water by Use of a Screen-Printed Carbon Electrode Modified with Chitosan-Crafted ZnO Nanoneedles. *J Colloid Interface Sci* **2017**, *499*, 83–92. https://doi.org/10.1016/j.jcis.2017.03.088.
35. Balasubramanian, P.; Balamurugan, T. S. T.; Chen, S. M.; Chen, T. W. Simplistic Synthesis of Ultrafine $CoMnO_3$ Nanosheets: An Excellent Electrocatalyst for Highly Sensitive Detection of Toxic 4-Nitrophenol in Environmental Water Samples. *J Hazard Mater* **2019**, *361*, 123–133. https://doi.org/10.1016/j.jhazmat.2018.08.070.
36. Peng, D.; Zhang, J.; Qin, D.; Chen, J.; Shan, D.; Lu, X. An Electrochemical Sensor Based on Polyelectrolyte-Functionalized Graphene for Detection of 4-Nitrophenol. *Journal of Electroanalytical Chemistry* **2014**, *734*, 1–6. https://doi.org/10.1016/j.jelechem.2014.09.027.
37. Sajjan, V. A.; Aralekallu, S.; Nemakal, M.; Palanna, M.; Keshavananda Prabhu, C. P.; Koodlur Sannegowda, L. Nanomolar Detection of 4-Nitrophenol Using Schiff-Base Phthalocyanine. *Microchemical Journal* **2021**, *164*. https://doi.org/10.1016/j.microc.2021.105980.
38. Laugier, J.; Bochu, B. CHECKCELL. Laboratoire des Matériaux et du Génie Physique Ecole Nationale Supérieure de Physique de Grenoble (INPG): Grenoble October 22, 2010. https://www.inpg.fr/LMGP (accessed 2024-06-05).
39. Rodríguez-Carvajal, J. Recent Advances in Magnetic Structure Determination by Neutron Powder Diffraction. *Physica B: Physics of Condensed Matter* **1993**, *192* (1–2), 55–69. https://doi.org/10.1016/0921-4526(93)90108-I.
40. Inc., B. A. X. I. SMART, SAINTPLUS V6.02, SHELXTL V6.10 and SADABS; Bruker Analytical X-Ray Instruments Inc., Madison, Wisconsin, USA. 2015.
41. Sheldrick, G.M. SHELXL-97. Program for the Refinement of Crystal Structures; University of Göttingen: Stuttgart, Germany. Program for the Refinement of Crystal Structures. University of Göttingen,. 1997.
42. Dolomanov, O. V.; Bourhis, L. J.; Gildea, R. J.; Howard, J. A. K.; Puschmann, H. OLEX2: A Complete Structure Solution, Refinement and Analysis Program. *J Appl Crystallogr* **2009**, *42* (2), 339–341. https://doi.org/10.1107/S0021889808042726.
43. Raccah, P. M.; Bouchard, R. J.; Wold, A. Crystallographic Study of Chromium Spinels. *J Appl Phys* **1966**, *37* (3), 1436–1437. https://doi.org/10.1063/1.1708502.
44. Baur, W. H. The Geometry of Polyhedral Distortions. Predictive Relationships for the Phosphate Group. *Acta Crystallogr B* **1974**, *30* (5), 1195–1215. https://doi.org/10.1107/S0567740874004560.
45. Wildner, M. On the Geometry of $Co(II)O_6$ in Inorganic Compounds. *Zeitschrift für Kristallographie* **1992**, *202*, 51–70. https://doi.org/10.1524/zkri.1992.202.1-2.51.
46. Robinson K; Gibbs GV; Ribbe PH. Quadratic Elongation: A Quantitative Measure of Distortion in Coordination Polyhedra. *Science (1979)* **1971**, *172* ((3983)), 567–570.
47. López-Vergara, F.; Galdámez, A.; Manríquez, V.; González, G. Crystal Structure and Raman Scattering Characterization of $Cu_2Fe_{1-x}Co_xSnS_4$ Chalcogenide Compounds. *Solid State Sci* **2015**, *49*, 54–60. https://doi.org/10.1016/j.solidstatesciences.2015.09.010.
48. Shannon, R. D. Revised Effective Ionic Radii and Systematic Studies of Interatomic Distances in Halides and Chalcogenides. *Acta Crystallographica Section A* **1976**, *32* (5), 751–767. https://doi.org/10.1107/S0567739476001551.
49. Gibart, M. P.; Robbins, M.; Lambrecht, V. G. NEW FERRIMAGNETIC SPINEL COMPOSITIONS IN THE SYSTEM $MCr_2S_{4-x}Se_x$ WHERE M=Fe, Co, Mn; Pergamon Press, 1973; Vol. 34.
50. Smilgies, D. M. Scherrer Grain-Size Analysis Adapted to Grazing-Incidence Scattering with Area Detectors. *J Appl Crystallogr* **2009**, *42* (6), 1030–1034. https://doi.org/10.1107/S0021889809040126.